




Cite this: *RSC Adv.*, 2020, 10, 22606

# Hierarchical $\text{Co}(\text{OH})_2@ \text{NiMoS}_4$ nanocomposite on carbon cloth as electrode for high-performance asymmetric supercapacitors†

Junxian Li, Jianwei Zhao, \* Lirong Qin,  Qitao Zhang, Xiaolan Tang and Yingying Xu

Hierarchical  $\text{Co}(\text{OH})_2@ \text{NiMoS}_4$  nanocomposites were successfully prepared on a carbon cloth by using a simple two-step hydrothermal method coupled with a room-temperature vulcanization method. The resulting nanocomposites were composed of large-scale uniform  $\text{Co}(\text{OH})_2$  nanowires fully covered with ultrathin vertical  $\text{NiMoS}_4$  nanoflakes. Because of the synergetic effect between  $\text{Co}(\text{OH})_2$  and  $\text{NiMoS}_4$ , the nanocomposites exhibited good electrochemical performance as a supercapacitor electrode. In particular, a specific capacity of  $2229 \text{ F g}^{-1}$  was achieved at a current density of  $1 \text{ A g}^{-1}$ . In addition, an asymmetrical supercapacitor fabricated using activated carbon as the negative electrode and the as-synthesised nanocomposite as the positive electrode exhibited a maximum energy density of  $59.5 \text{ W h kg}^{-1}$  at a power density of  $1 \text{ kW h kg}^{-1}$  and excellent cycling stability (100% capacitance retention after 5000 cycles). These results indicate that the hierarchical  $\text{Co}(\text{OH})_2@ \text{NiMoS}_4$  nanocomposite has great potential for practical application in high-performance energy storage devices.

Received 11th April 2020

Accepted 8th June 2020

DOI: 10.1039/d0ra03253k

rsc.li/rsc-advances

## Introduction

Supercapacitors, a new type of energy storage device, exhibit higher power and energy densities and better cycling stability compared with traditional energy storage devices and thus have wide applications in portable electronic equipment, electric vehicles, and high-power supplies.<sup>1,2</sup> The design and synthesis of novel electrode materials to achieve a higher energy density is a key aspect in extending the application scope of supercapacitors.<sup>3–5</sup> Therefore, in recent years, many kinds of electrode materials such as hydroxides, sulphides, and transition metal oxides have been investigated for application as supercapacitor electrodes.<sup>6,7</sup> Among these, sulphides (*e.g.*,  $\text{Co}_3\text{S}_4$ ,  $\text{NiS}_2$ , and  $\text{MoS}_2$ )<sup>8–10</sup> have shown superior performance in terms of electron transmission capacity, electronegativity, and mechanical and thermal stability, and offer a more flexible structure and better cycling stability and rate capacity compared with conventional energy storage materials.<sup>11,12</sup> In particular, ternary transition metal sulphides have attracted widespread attention as they can facilitate rich redox reactions and have high electrical conductivity and are considered promising candidates for energy storage materials.<sup>13</sup> Chen *et al.*<sup>14</sup> successfully prepared  $\text{NiCo}_2\text{S}_4$  urchin-like nanostructures using nickel sulphide and cobalt bases, which delivered a specific

capacitance of  $1149 \text{ F g}^{-1}$  at a current density of  $1 \text{ A g}^{-1}$ . Fan *et al.*<sup>15</sup> synthesised a three-dimensional  $\text{NiCo}_2\text{S}_4$ -rGO hierarchical porous structure by the hydrothermal method and achieved a high specific capacitance of  $1107 \text{ F g}^{-1}$  at a current density of  $1 \text{ A g}^{-1}$  that decreased by only 10% after 5000 cycles. Du *et al.*<sup>16</sup> synthesized a  $\text{NiMoS}_4$ -A compound by a chemical coprecipitation method and obtained a high specific capacity of  $313 \text{ C g}^{-1}$  at  $1 \text{ A g}^{-1}$  and a high energy density of  $35 \text{ W h kg}^{-1}$  at a power density of  $400 \text{ W kg}^{-1}$ .

These studies demonstrate that composite electrode materials can further increase the rate capacity and cycling stability because of their structural advantages. Sulphide-based composite materials<sup>17</sup> such as hydroxide and sulphide composites,<sup>18</sup> ternary sulphide and metal sulphide composites,<sup>19</sup> and a series of other multi-component nanomaterials<sup>20</sup> have been explored.  $\text{Co}(\text{OH})_2$  is a suitable candidate for electrode materials because of its unique layered structure, abundance, environmental benignity, and high theoretical capacitance.<sup>21,22</sup> Xu's group successfully prepared a three-dimensional  $\text{Ni-Co-S/Co}(\text{OH})_2$  nanocomposite using  $\text{Co}(\text{OH})_2$  as a precursor and achieved a high specific capacitance of  $1560.8 \text{ F g}^{-1}$  and an energy density of  $48.8 \text{ W h Kg}^{-1}$  at a power density of  $800 \text{ W kg}^{-1}$ , which indicate its superior performance as a supercapacitor.<sup>18</sup> Nevertheless, studies on transition metal sulphides/hydroxides as supercapacitor electrodes are still rare, and further studies are required to improve the performance of supercapacitors. In this study, a new composite electrode material,  $\text{Co}(\text{OH})_2$  nanowires@ $\text{NiMoS}_4$  nanoflakes, with a heterogeneous structure was successfully prepared on

School of Physical Science and Technology, Southwest University, Chongqing 400715, P. R. China. E-mail: zhaojw@swu.edu.cn

† Electronic supplementary information (ESI) available. See DOI: 10.1039/d0ra03253k



a carbon cloth by a simple two-step hydrothermal method coupled with a room-temperature vulcanization method. This unique hierarchical structure increased the number of active sites and facilitated the transport of a large number of electrolyte ions.<sup>23,24</sup> Moreover, because of the low electronegativity of sulphur ions, the electrical conductivity of the electrode material increased. And, the incorporated Mo element could further decrease the charge transfer resistance of the electrodes, thus leading to an increased power density. An asymmetric supercapacitor (ASC) fabricated using activated carbon (AC) as the negative electrode and the as-synthesised nanocomposite as the positive electrode exhibited a good electrochemical performance, with a high energy density of 59.5 W h Kg<sup>-1</sup> at a power density of 1000 W Kg<sup>-1</sup> and an excellent cycling stability with 100% capacitance retention after 5000 cycles. The originality and novelty of this work is to introduce a new strategy in structural engineering for developing highly efficient energy storage devices.

## Experimental section

### Growth of Co(OH)<sub>2</sub> nanowires on carbon cloth

All the reagents were of analytical grade and used without further purification. A piece of carbon cloth 3 × 3 cm<sup>2</sup> in size was thoroughly ultrasonically washed in absolute ethanol and deionised water for 15 min, and then dried at room temperature. The typical synthesis process was as follows: 0.873 g of Co(NO<sub>3</sub>)<sub>2</sub>·6H<sub>2</sub>O (3 mmol), 0.09 g of CO(NH<sub>2</sub>)<sub>2</sub> (1.5 mmol), and 0.21 g of C<sub>6</sub>H<sub>12</sub>N<sub>4</sub> (1.5 mmol) were dissolved in 30 mL of deionised water by continuous vigorous stirring to obtain a clear solution. Next, the washed carbon cloth and solution were transferred to a 50 mL Teflon-lined stainless autoclave that was then sealed and maintained at 120 °C for *t*<sub>1</sub> = 4 h. After cooling to room temperature naturally, the product was taken out and washed in ethanol and deionised water several times. Finally, the sample was dried at 60 °C for 12 h to obtain Co(OH)<sub>2</sub> nanowires on carbon cloth.

### Growth of NiMoS<sub>4</sub> nanoflakes on Co(OH)<sub>2</sub> nanowires

First, 0.872 g of Ni(NO<sub>3</sub>)<sub>2</sub>·6H<sub>2</sub>O (3 mmol), 1.936 g of Na<sub>2</sub>MoO<sub>4</sub>·2H<sub>2</sub>O (8 mmol), 0.09 g of CO(NH<sub>2</sub>)<sub>2</sub> (1.5 mmol), and 0.21 g of C<sub>6</sub>H<sub>12</sub>N<sub>4</sub> (1.5 mmol) were dissolved in 30 mL of deionised water by magnetic stirring to obtain a clear solution. The solution and the carbon cloth with the Co(OH)<sub>2</sub> nanowires were transferred to a 50 mL Teflon-lined stainless autoclave and heated at 120 °C for different periods (*t*<sub>2</sub> = 2, 4, and 6 h) to determine the optimum reaction conditions. Afterwards, the carbon cloth was taken out, washed several times with deionised water and ethanol, and dried at 60 °C for 12 h to obtain a Co(OH)<sub>2</sub>/Ni-Mo oxy-hydroxide (denoted as NiMo-O(OH)) composite precursor on carbon cloth. The precursor was then immersed in a 33 wt% Na<sub>2</sub>S solution for *t*<sub>3</sub> = 12 h for *in situ* vulcanization. Finally, the product was taken out, washed in ethanol and deionised water several times, and dried at 60 °C for 12 h to obtain Co(OH)<sub>2</sub>@NiMoS<sub>4</sub> nanocomposite on carbon cloth. The mass loadings of the Co(OH)<sub>2</sub>@NiMoS<sub>4</sub> composite

on carbon cloth after 2, 4, and 6 h were 3.1, 3.5, and 4.1 mg cm<sup>-2</sup>, respectively. For comparison, CoS<sub>2</sub> nanowires were prepared on a carbon cloth by the *in situ* vulcanization of Co(OH)<sub>2</sub> nanowires on carbon cloth.

### Material characterisation

The microstructures and morphologies of the Co(OH)<sub>2</sub>@NiMoS<sub>4</sub> nanocomposites were analysed by field emission scanning electron microscopy (FESEM) and energy dispersive X-ray spectroscopy (EDS) using a field emission scanning electron microscope equipped with an energy dispersive X-ray spectrometer (JEOL JSM-7100F), and high-resolution transmission electron microscopy (HRTEM, FEI Tecnai G20) equipped with selected area electron diffraction (SAED) patterns. The elemental compositions of the as-synthesised products were determined by X-ray photoelectron spectroscopy (XPS, Thermo Scientific ESCALAB250).

### Electrochemical measurements

The electrochemical tests were carried out at room temperature using a CHI 660E three-electrode system electrochemical workstation (CH Instruments, China). The as-synthesised nanocomposite (1 cm × 1 cm), a Pt wire electrode, and an Ag/AgCl electrode were used as the working, counter, and reference electrodes, respectively. A 3.0 M KOH solution was used as the electrolyte. Cyclic voltammetry (CV), galvanostatic charge-discharge (GCD) tests, and electrochemical impedance spectroscopy were performed. The specific capacitance of the sample was calculated by the following equation:<sup>25</sup>

$$C_m = \frac{I \times \Delta t}{m \times \Delta V}, \quad (1)$$

where *C*<sub>m</sub>, *I*, Δ*t*, Δ*V*, and *m* represent the specific capacitance (F g<sup>-1</sup>), discharge current (A), discharge time (s), potential window (V), and total active material mass (g), respectively.

### Fabrication of asymmetric supercapacitor (ASC)

Asymmetric supercapacitors (ASCs) were fabricated using the Co(OH)<sub>2</sub>@NiMoS<sub>4</sub> nanocomposites on carbon cloth as the positive electrode and AC as the negative electrode. The AC electrode was prepared by mixing AC, conductive carbon black, and polytetrafluoroethylene emulsion in a weight ratio of 80 : 10 : 10 with stirring to form a homogeneous slurry. The slurry was then painted onto a washed Ni foam (1 cm × 1 cm) and dried at 60 °C for 10 h in a vacuum oven. Finally, the resultant electrodes were pressed at 10 MPa to form a sheet electrode. In a two-electrode system, CV and GCD tests were performed with 3 M KOH as the electrolyte. The specific capacitance (*C*<sub>s</sub>), energy density (*E*), and power density (*P*) of the ASCs were calculated by the following equations:<sup>26</sup>

$$\frac{m^+}{m^-} = \frac{C_- \times \Delta V}{C_+ \times \Delta V} \quad (2)$$

$$C_s = \frac{I \times \Delta t}{M \times \Delta V} \quad (3)$$



$$E = \frac{1}{2} C_s \Delta V^2 \quad (4)$$

$$P = \frac{E}{\Delta t} \quad (5)$$

Here,  $m_{\pm}$  and  $C_{\pm}$  represent the active material mass and specific capacitance of the positive (or negative) electrode, respectively,  $\Delta V$  is the potential window,  $I$  is the discharge current (A),  $\Delta t$  is the discharge time (s), and  $M$  is the total mass (g) of the two electrodes.

## Results and discussion

### Material characterisation

The synthesis process of the  $\text{Co}(\text{OH})_2 @ \text{NiMoS}_4$  nanocomposites is illustrated in Fig. 1a. In the first step,  $\text{Co}(\text{OH})_2$  nanowires were grown on a carbon cloth by a hydrothermal method. The SEM image of the  $\text{Co}(\text{OH})_2$  nanowires grown on a carbon cloth is shown in Fig. 1b. As can be seen, a large number of  $\text{Co}(\text{OH})_2$  nanowires uniformly cover the entire surface of the carbon fibres forming clusters of a slender interlaced structure. The average length of these nanowires is 10  $\mu\text{m}$  or less. The corresponding high-magnification SEM image (Fig. 1c) shows that

each nanowire has a uniform diameter and a smooth surface. The diameter of the nanowires is approximately 40–100 nm. More SEM images of the  $\text{Co}(\text{OH})_2$  nanowires can be seen in Fig. S1 (ESI†). The chemical composition of the nanowires was determined by EDS. Combining these findings with previous reports leads to the deduction that the strong Co and O peaks in the corresponding EDS spectrum (Fig. 1d) indicate the formation of  $\text{Co}(\text{OH})_2$ . The as-grown  $\text{Co}(\text{OH})_2$  nanowires on the carbon fibres formed a three-dimensional brush-like structure that increased the specific surface area of the active material. In the second step, Ni–Mo oxy-hydroxide nanoflakes were grown on the  $\text{Co}(\text{OH})_2$  nanowires. The SEM image of the Ni–Mo oxy-hydroxide nanoflakes synthesized by 4 h of hydrothermal reaction is shown in Fig. 1e. As can be seen, many wire-like structures cover the entire surface of the carbon fibres, as in the case of  $\text{Co}(\text{OH})_2$  nanowires shown in Fig. 1b. The average length of these wire-like structures is 10  $\mu\text{m}$ . The high-magnification SEM image (Fig. 1f) shows that the wire-like structure is composed of highly dense and uniform nanoflakes distributed on the  $\text{Co}(\text{OH})_2$  nanowires. Hence, the diameter of the composite wire-like structure is 200–300 nm. The nanoflakes are a few nanometres in thickness and tens of nanometres in lateral size. These small flakes are interlaced and

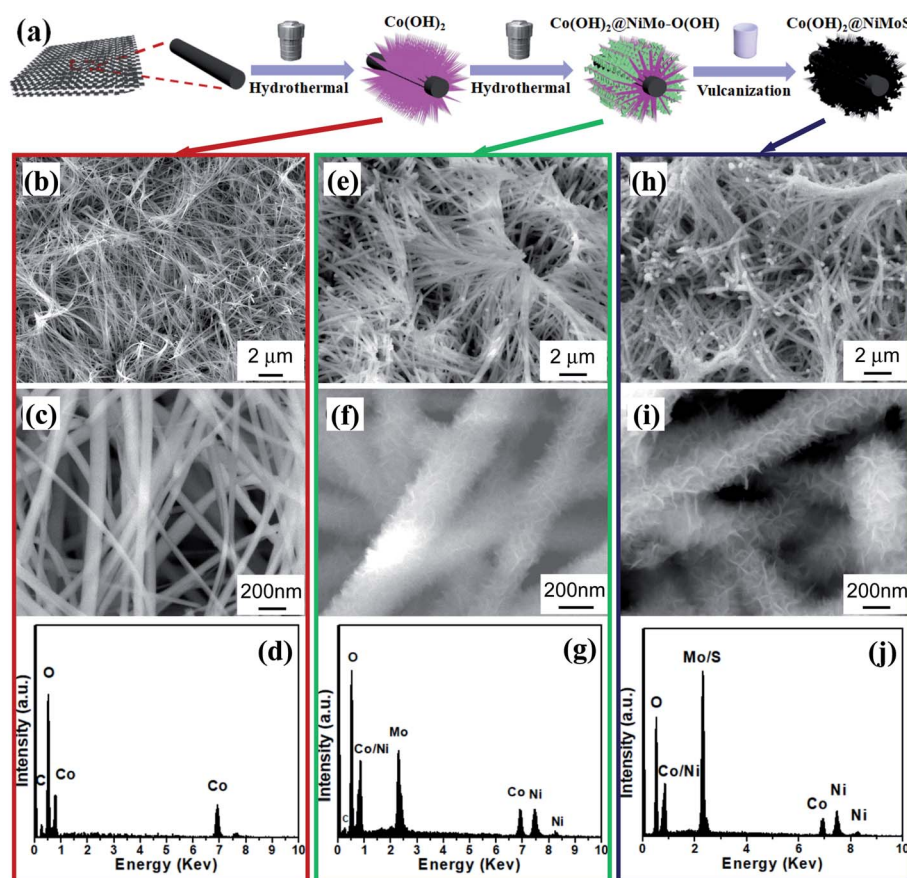


**Fig. 1** (a) Schematic of the synthesis process of  $\text{Co}(\text{OH})_2 @ \text{NiMoS}_4$  nanocomposites; (b) low- and (c) high-magnification SEM images of  $\text{Co}(\text{OH})_2$  nanowires grown on carbon cloth and (d) EDS spectrum of  $\text{Co}(\text{OH})_2$  nanowires; (e) low- and (f) high-magnification SEM images of Ni–Mo oxy-hydroxide nanoflakes grown on  $\text{Co}(\text{OH})_2$  nanowires for 4 h and (g) EDS spectrum of Ni–Mo oxy-hydroxide nanoflakes; (h) low- and (i) high-magnification SEM images of  $\text{Co}(\text{OH})_2 @ \text{NiMoS}_4$  nanocomposite and (j) EDS spectrum of  $\text{Co}(\text{OH})_2 @ \text{NiMoS}_4$  nanocomposite.





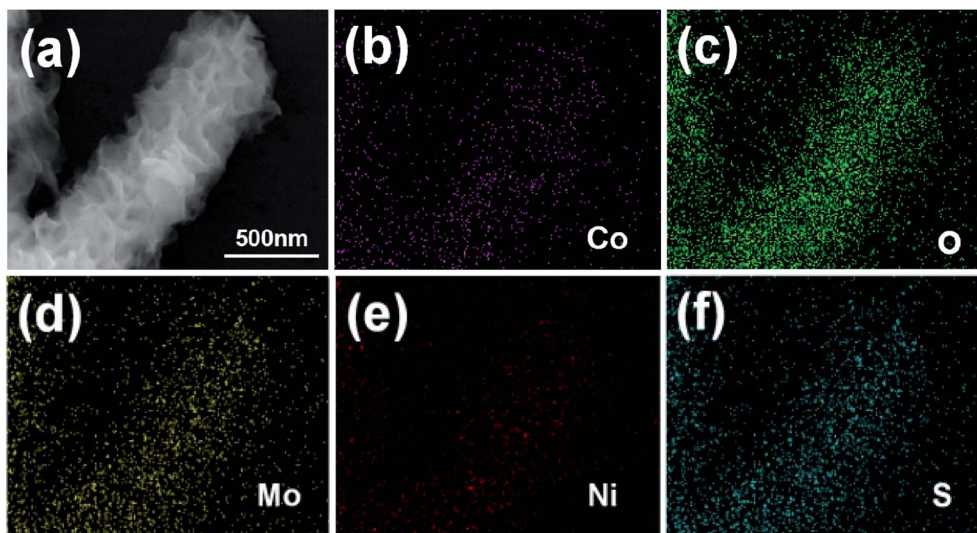


Fig. 2 (a) SEM image of  $\text{Co(OH)}_2\text{@NiMoS}_4$  nanocomposite, and (b)–(f) element mapping images of Co, O, Mo, Ni, and S.

form a three-dimensional structure with open spaces, offering a large specific surface area.<sup>19</sup> The corresponding EDS spectrum (Fig. 1g) shows that the product obtained in the second step is composed of O, Mo, Co, and Ni. According to our previous work,<sup>5</sup> these nanoflakes should be Ni–Mo oxy-hydroxide.

In the third step, the nanoflake precursors were vulcanized *in situ* at room temperature. After vulcanization, the overall appearance of the final product was similar to that of the sample obtained in the second step, as shown in Fig. 1h and i. The average length of the wire-like structures in the final product remained the same (approximately 10  $\mu\text{m}$ ). However, the lateral size and thickness of the nanoflakes grown on the  $\text{Co(OH)}_2$  nanowires increased slightly, which indicates a tiny increase of surface area after

sulfuration. Although the major peaks of S and Mo overlap in the EDS spectrum (shown in Fig. 1j), the increase in peak intensity indicates a change in material composition after vulcanization. The above speculation can be confirmed by the corresponding XRD analysis illustrated in Fig. S2 (ESI<sup>†</sup>). It indicates the formation of  $\text{Co(OH)}_2$  in the first step, and the growth of  $\text{Ni(OH)}_2$  and  $\text{MoO}_2$  composites in the second step. After vulcanization, the XRD peaks corresponding to  $\text{Co(OH)}_2$  still remain, showing the preserve of  $\text{Co(OH)}_2$  nanowires. On the contrary, all of the peaks corresponding to  $\text{Ni(OH)}_2$  and  $\text{MoO}_2$  has disappeared to be replaced by some new peaks, which can be attributed to the formation of  $\text{NiMoS}_4$ .<sup>27</sup> The weight ratio of  $\text{NiMoS}_4$  to  $\text{Co(OH)}_2$  for the final product ( $t_2 = 4$  h) is about 4 : 5 by precision weighing method.

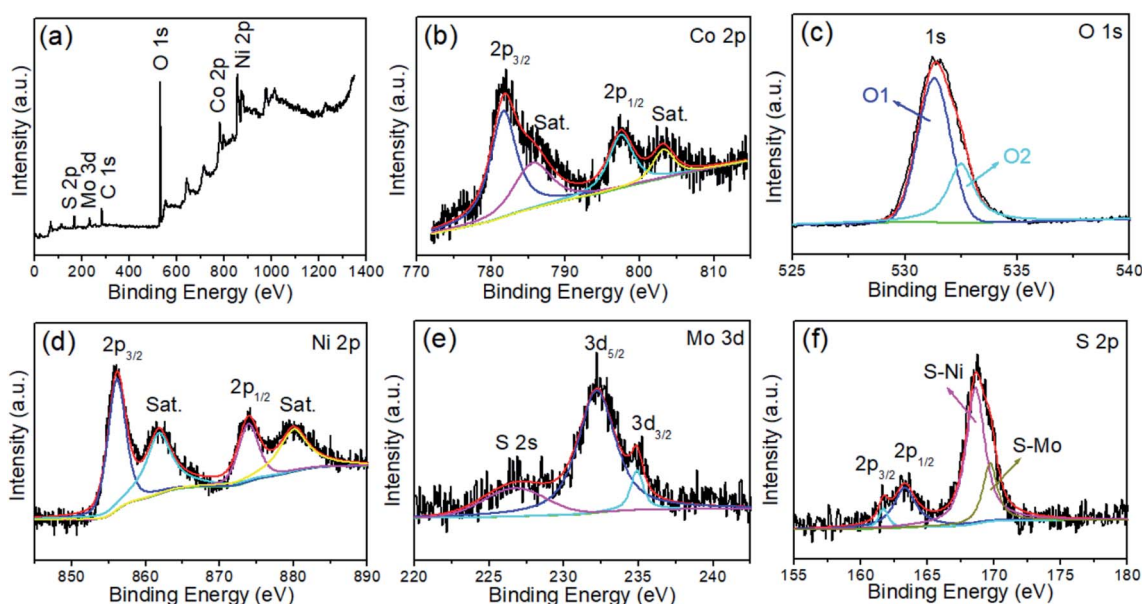


Fig. 3 (a) XPS survey spectrum, and high-resolution XPS spectra of (b) Co 2p, (c) O 1s, (d) Ni 2p, (e) Mo 3d, (f) S 2p of  $\text{Co(OH)}_2\text{@NiMoS}_4$  nanocomposite. The satellite peaks are denoted as "Sat.".

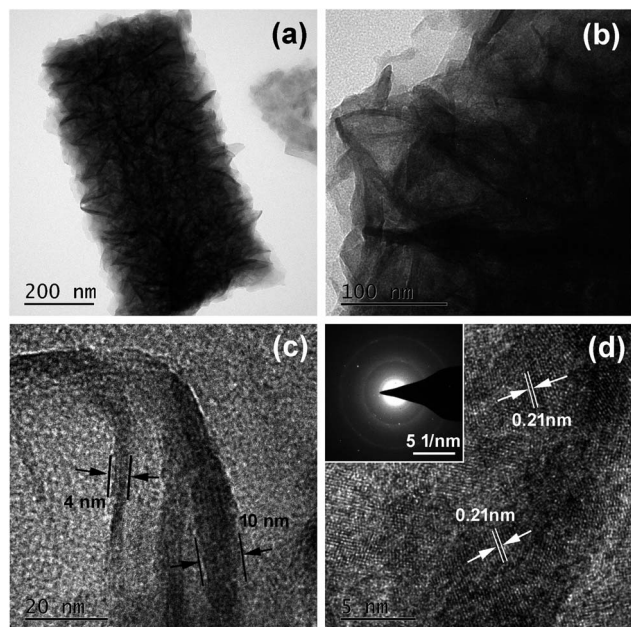


Fig. 4 (a)–(c) TEM images and (d) HRTEM image of  $\text{Co(OH)}_2\text{@NiMoS}_4$  nanocomposite. The inset of (d) shows the corresponding SAED pattern.

The spatial distributions of specific elements in the composite were determined by EDS elemental mapping analysis. As can be seen in Fig. 2, Co and O are distributed primarily in the core region, while Mo, Ni, and S are uniformly distributed in the entire nanocomposite. The elemental composition and valence states of the elements near the surface of the  $\text{Co(OH)}_2\text{@NiMoS}_4$  nanocomposites were determined by XPS. The XPS survey spectrum in Fig. 3a shows the presence of Ni, Co, Mo, O, and S in the sample, consistent with the EDS elemental mapping results. The C peak originates from the carbon fibres used as the substrate. The high-resolution spectra were fitted using a Gaussian curve-fitting method. The Co 2p spectrum (Fig. 3b) deconvoluted into two peaks at binding energies of 781.7 ( $2p_{3/2}$ ) and 797.5 eV ( $2p_{1/2}$ ) that are attributed to  $\text{Co}^{2+}$ . In addition, two shake-up satellites peaks (labelled as

“Sat.”) appeared at 785.6 and 803.2 eV.<sup>28</sup> The O 1s XPS spectrum (Fig. 3c) deconvoluted into two peaks labelled as O1 and O2. The O1 peak at 531.3 eV is generally ascribed to  $\text{OH}^-$  groups, which indicates the formation of hydroxide.<sup>29</sup> Thus, the nanowires obtained in the first synthetic step was confirmed to be  $\text{Co(OH)}_2$ . The O2 peak at 532.5 eV is attributed to the multiplicity of adsorbed water at or near the surface.<sup>28</sup> The Ni 2p spectrum (Fig. 3d), deconvoluted into two main peaks at binding energies of 856.1 ( $2p_{3/2}$ ) and 873.9 eV ( $2p_{1/2}$ ) that are attributed to  $\text{Ni}^{2+}$ , while the corresponding satellite peaks at 861.8 and 880.0 eV are ascribed to  $\text{Ni}^{3+}$  or  $\text{Ni}^{4+}$  active species.<sup>30</sup> The high-resolution Mo 3d spectrum (Fig. 3e) overlaps with the S 2s region and deconvoluted into two peaks at 232.1 and 235.1 eV corresponding to Mo  $3d_{5/2}$  and  $3d_{3/2}$ , respectively. The two peaks are separated by a splitting width of approximately 3.1 eV, which is characteristic of the  $\text{Mo}^{6+}$  oxidation state.<sup>31</sup> The S 2p spectrum (Fig. 3f) deconvoluted into peaks at 161.7 ( $2p_{3/2}$ ) and 163.3 eV ( $2p_{1/2}$ ), which confirm the presence of terminal  $\text{S}^{2-}$  ions. The peaks at 168.6 and 169.7 eV originate from S–Ni and S–Mo, respectively.<sup>32</sup> The XPS analysis results demonstrate the presence of  $\text{Co}^{2+}$ ,  $\text{Ni}^{2+}$ , and  $\text{Mo}^{6+}$  in the final products, indicating the successful synthesis of  $\text{Co(OH)}_2\text{@NiMoS}_4$  nanocomposites.

The TEM image in Fig. 4a shows that the diameter of a single  $\text{Co(OH)}_2\text{@NiMoS}_4$  nanocomposite structure is approximately 400 nm. Moreover, many nanoflakes are attached to the central axis, forming a section of wire-like structure; this is consistent with the SEM observations. The magnified TEM image in Fig. 4b shows that these nanoflakes are interconnected and form a highly porous network structure that can considerably shorten the electron and ion transport pathways, resulting in a superior electrochemical reaction activity. Fig. 4c shows that the thickness of these nanoflakes is approximately 4–10 nm. The HRTEM image in Fig. 4d shows lattice fringes with interplanar spacings of 0.21 nm and 0.15 nm corresponding to the (220) and (110) crystal planes of  $\text{NiS}_2$  and  $\text{MoS}_2$ , respectively. This reveals that  $\text{NiMoS}_4$  contains  $\text{NiS}_2$  and  $\text{MoS}_2$ .<sup>14</sup> The SAED pattern showing well-defined rings (inset of Fig. 4d) indicates the polycrystalline nature of the  $\text{CoMoS}_4$  nanocomposites.

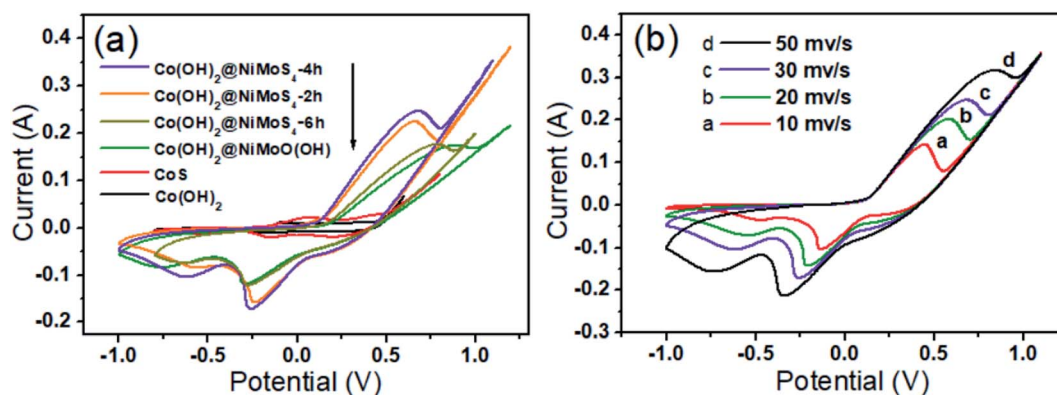


Fig. 5 (a) CV curves of  $\text{Co(OH)}_2$ ,  $\text{CoS}$ ,  $\text{Co(OH)}_2\text{@NiMo-O(OH)}$ , and  $\text{Co(OH)}_2\text{@NiMoS}_4$  prepared for different reaction times in the second stage ( $t_2 = 2, 4$  and  $6$  h) measured at a scan rate of  $30 \text{ mV s}^{-1}$ . (b) CV curves of  $\text{Co(OH)}_2\text{@NiMoS}_4$ -4 h electrode measured at different scanning rates.





## Electrochemical properties of the nanocomposites

The electrochemical performance of  $\text{Co}(\text{OH})_2$ ,  $\text{CoS}_2$ ,  $\text{Co}(\text{OH})_2@-\text{NiMo}-\text{O}(\text{OH})$ , and  $\text{Co}(\text{OH})_2@-\text{NiMoS}_4$  synthesized for different reaction times in the second stage ( $t_2 = 2, 4$ , and 6 h) were evaluated by CV performed at a scan rate of  $30 \text{ mV s}^{-1}$  using a 3.0 M KOH solution as the electrolyte in a three-electrode system. The appearance of strong redox peaks in the CV curves (Fig. 5a) indicates a good pseudo-capacitive behaviour originating from the faradaic redox reactions.<sup>33</sup> Notably, among all the synthesized electrode materials, the  $\text{Co}(\text{OH})_2@-\text{NiMoS}_4$  electrode sample prepared for  $t_2 = 4 \text{ h}$  ( $\text{Co}(\text{OH})_2@-\text{NiMoS}_4\text{-4 h}$ ) exhibits the largest hysteresis loop area in the CV curve. The higher specific capacitance of the  $\text{Co}(\text{OH})_2@-\text{NiMoS}_4$  electrodes can be attributed to their high electrical conductivity, large specific surface area, and the synergistic effect of the nanocomposite components.<sup>28</sup> The effect of scan rate on the performance of the  $\text{Co}(\text{OH})_2@-\text{NiMoS}_4\text{-4 h}$  nanocomposite used as the working electrode is shown in Fig. 5b. With an increase in scan rate from 10 to  $50 \text{ mV s}^{-1}$ , the cathodic and anodic peaks shifted towards more negative and positive potentials; however, the shapes of the CV curves did not change significantly. This indicates the good rate capability and low polarisation of the nanocomposite.<sup>34</sup> Furthermore, as determined by calculations, both the oxidation and reduction peak currents are proportional to the square root of the scanning rate, and diffusion is the dominant electrochemical process.<sup>5</sup>

Fig. 6a shows the GCD curves of the  $\text{Co}(\text{OH})_2@-\text{NiMoS}_4\text{-4 h}$  nanocomposite electrode measured at different current

densities (1, 2, 3, 5, and  $10 \text{ A g}^{-1}$ ) in the potential range of  $-0.1 \text{ V}$  to  $0.37 \text{ V}$ . The appearance of two pronounced potential plateaus during the charge–discharge cycles indicates the pseudo-capacitive behaviour of the reversible faradaic capacitance reaction. In addition, with an increase in current density, the discharge time gradually decreased, which indicates the high utilization rate of the composite electrode under a low current density.<sup>35</sup> The specific capacitance of the  $\text{Co}(\text{OH})_2@-\text{NiMoS}_4\text{-4 h}$  electrode at different current densities were calculated by eqn (1). The  $\text{Co}(\text{OH})_2@-\text{NiMoS}_4\text{-4 h}$  electrode delivered specific capacitances of 2229, 2094, 1989, 1797, and  $1436 \text{ F g}^{-1}$  ( $6.69, 6.28, 5.97, 5.39$ , and  $4.31 \text{ F cm}^{-2}$ ) at current densities of 1, 2, 3, 5, and  $10 \text{ A g}^{-1}$  (corresponding to 3, 6, 9, 15 and  $30 \text{ mA cm}^{-2}$ ), respectively. Moreover, at 5 and  $10 \text{ A g}^{-1}$ , the electrode retained 81% and 64% of the specific capacitance delivered at  $1 \text{ A g}^{-1}$ , respectively, which demonstrates its good rate performance. Accordingly, the specific capacitances of  $\text{Co}(\text{OH})_2$ ,  $\text{CoS}_2$ ,  $\text{Co}(\text{OH})_2@-\text{NiMo}-\text{O}(\text{OH})$ , and  $\text{Co}(\text{OH})_2@-\text{NiMoS}_4$  prepared for different hydrothermal times ( $t_2 = 2 \text{ h}$  and 6 h) were measured at different current densities. With an increase in current density from 1 to  $10 \text{ A g}^{-1}$ , the specific capacitance retentions of were 72, 57, 37, 59, and 47%, respectively (Fig. 6b). The  $\text{Co}(\text{OH})_2@-\text{NiMoS}_4\text{-4 h}$  composite electrode retains the highest specific capacitance and has higher capacitance retention throughout. Furthermore, the cycling stability of the electrode materials was evaluated by performing charge–discharge cycling tests for 2000 cycles at a constant current density of

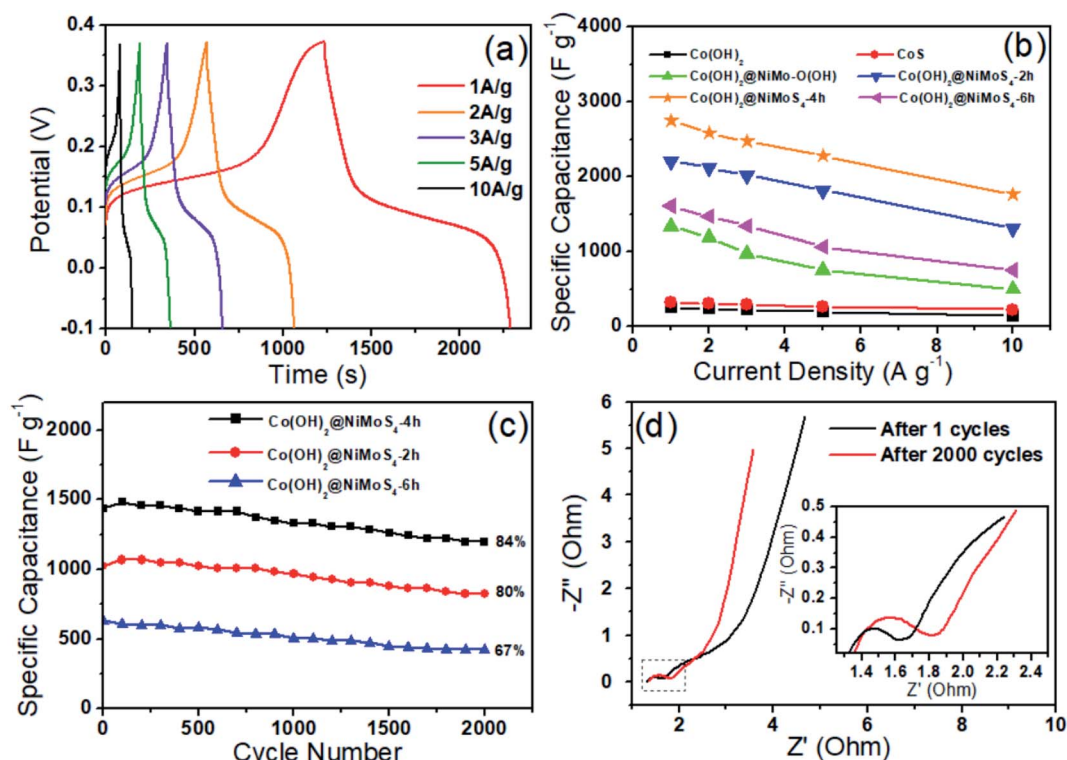


Fig. 6 (a) GCD curves of  $\text{Co}(\text{OH})_2@-\text{NiMoS}_4\text{-4 h}$  electrode at different current densities, (b) specific capacitances of  $\text{Co}(\text{OH})_2$ ,  $\text{CoS}_2$ ,  $\text{Co}(\text{OH})_2@-\text{NiMo}-\text{O}(\text{OH})$ , and  $\text{Co}(\text{OH})_2@-\text{NiMoS}_4$  electrodes at different current densities, (c) cycling performance of  $\text{Co}(\text{OH})_2@-\text{NiMoS}_4\text{-4 h}$  electrode at a current density of  $10 \text{ A g}^{-1}$ , and (d) Nyquist plots of  $\text{Co}(\text{OH})_2@-\text{NiMoS}_4\text{-4 h}$  after 1st and 2000th cycles.

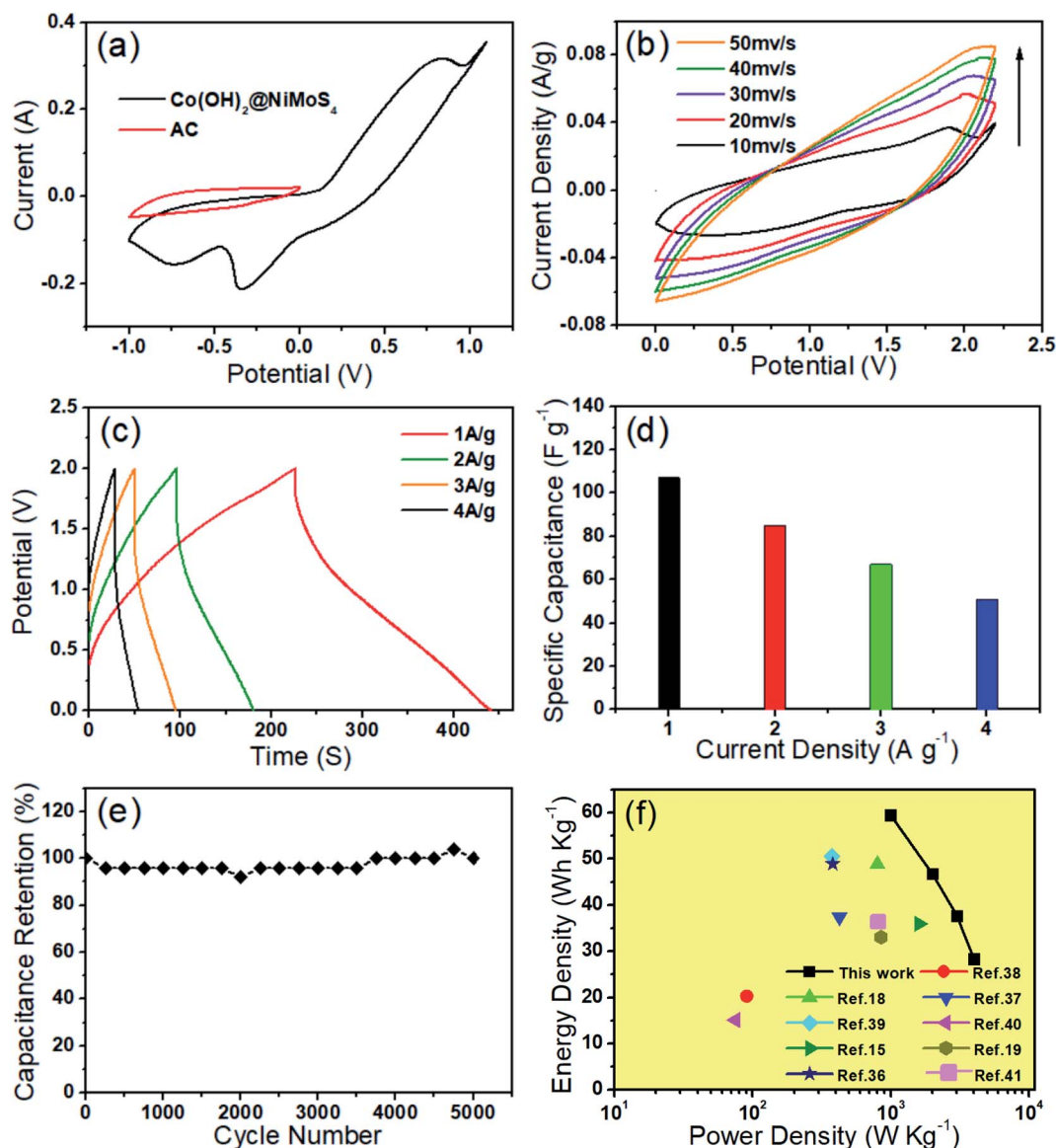


Fig. 7 (a) CV curves of AC and  $\text{Co(OH)}_2\text{@NiMoS}_4$ -4 h electrode at a scan rate of  $30 \text{ mV s}^{-1}$  in a three-electrode system, (b) CV curves of  $\text{Co(OH)}_2\text{@NiMoS}_4$ -4 h//AC capacitor at different scan rates from 10 to  $50 \text{ mV s}^{-1}$ , (c) GCD curves of the assembled capacitor at different current densities, (d) mass specific capacitance of the capacitor at different current densities, (e) cycling stability of the capacitor at current density of  $4 \text{ A g}^{-1}$  for 5000 cycles, (f) Ragone plots of energy density and power density of our  $\text{Co(OH)}_2\text{@NiMoS}_4$ -4 h//AC capacitor and comparison with other works.

$10 \text{ A g}^{-1}$ . As shown in Fig. 6c, the total capacitance retention of the  $\text{Co(OH)}_2\text{@NiMoS}_4$ -4 h electrode (approximately 84%) is higher than that of the  $\text{Co(OH)}_2\text{@NiMoS}_4$ -2 h electrode (approximately 80%) and  $\text{Co(OH)}_2\text{@NiMoS}_4$ -6 h electrode (approximately 67%). This indicates the excellent electrochemical performance of the  $\text{Co(OH)}_2\text{@NiMoS}_4$ -4 h nanocomposite. Moreover, the capacitance of the  $\text{Co(OH)}_2\text{@NiMoS}_4$ -4 h nanocomposite electrode decreased because of the slight increase in charge-transfer resistance during the charge-discharge process, as observed from the Nyquist plots of the nanocomposite after the 1st and 2000th cycles (Fig. 6d).<sup>7</sup> However, the diameter of the semicircle in the high-frequency region that corresponds to the charge-transfer resistance at

the electrolyte/electrode interface increased slightly after 2000 cycles (the inset of Fig. 6d), which indicates the good stability of the nanocomposite.<sup>13</sup>

Overall, the  $\text{Co(OH)}_2\text{@NiMoS}_4$ -4 h composite electrode demonstrated excellent capacitive performance, good cycling stability, and good rate capability, and thus has the potential for application in energy storage devices. The excellent properties of  $\text{Co(OH)}_2\text{@NiMoS}_4$  nanocomposites can be attributed to the following factors. First, the interlaced  $\text{Co(OH)}_2$  nanowires covered with the dense  $\text{NiMoS}_4$  nanoflakes form as a three-dimensional hierarchical structure that can provide a large surface area and more exposed electroactive sites, thereby shortening the ion diffusion path and increasing the specific



capacitance.<sup>36</sup> Second, metal sulphides have higher electrochemical activity and electrical conductivity than metal oxides or hydroxides,<sup>11,13</sup> while ternary transition metal sulphides offer richer redox reactions and have higher electrical conductivity than binary metal sulphides. Moreover, the interconnected NiMoS<sub>4</sub> nanoflakes provide more electron transport pathways and improve the electrical conductivity, thus delivering a higher capacitance. Finally, the Co(OH)<sub>2</sub>@NiMoS<sub>4</sub> composite was grown directly on a carbon cloth, which obviates the necessity of using a polymer binder for electrode preparation and ensures good structural integrity and fast electron transport.<sup>28</sup>

### Properties of the asymmetric supercapacitor (ASC)

To explore the feasibility of using the prepared nanocomposite as a supercapacitor electrode, an ASC was assembled using AC as the negative electrode, Co(OH)<sub>2</sub>@NiMoS<sub>4</sub>-4 h as the positive electrode, and 3 M KOH as the electrolyte according to a previously reported method. To determine the optimal cell voltage window for the assembled ASC, CV was performed using a three-electrode system with Co(OH)<sub>2</sub>@NiMoS<sub>4</sub>-4 h and AC as the electrodes. As can be seen in Fig. 7a, the CV curve of AC is rectangular in the potential range of -1.0 V to 0.0 V, which indicates that it is an electric double-layer capacitor. The CV of Co(OH)<sub>2</sub>@NiMoS<sub>4</sub>-4 h was measured in the potential range of -1.0 V to 1.1 V; thus, the potential window could be extended to 0.0–2.1 V. Fig. 7b shows the CV curves of the assembled ASC at different scanning rates ranging from 10 to 50 mV s<sup>-1</sup>. The CV curves of the ASC comprising the electric double-layer electrode and the pseudo-capacitive electrode show characteristic shapes. In addition, the shapes of the CV curves changed only slightly, which suggests the good performance of the nanocomposite capacitor.<sup>37,38</sup>

GCD tests were performed for the Co(OH)<sub>2</sub>@NiMoS<sub>4</sub>//AC capacitor at different current densities (1, 2, 3, and 4 A g<sup>-1</sup>) in the potential range of 0.0–2.0 V. The GCD curves are nearly symmetrical and linear, which indicates the excellent capacitive behaviour of the device (Fig. 7c). The specific capacitance of the ASC was calculated by eqn (3). As shown in Fig. 7d, the specific capacitances are 107.4, 84.5, 67.7, and 51.3 F g<sup>-1</sup> at current densities of 1, 2, 3, and 4 A g<sup>-1</sup>, respectively. The cycling stability of the Co(OH)<sub>2</sub>@NiMoS<sub>4</sub>//AC capacitor was evaluated by conducting GCD tests for 5000 cycles at a current density of 4 A g<sup>-1</sup>; the results are shown in Fig. 7e. As can be seen, the capacitance decreased slightly at the initial stage of the GCD test and then increased gradually. The capacitance retention rate was 100% after 5000 cycles; this indicates the excellent cycling stability of the ASC. Fig. 7f shows the Ragone plots of the Co(OH)<sub>2</sub>@NiMoS<sub>4</sub>//AC capacitor device calculated by eqn (4) and (5) and those of previously reported capacitors. The Co(OH)<sub>2</sub>@NiMoS<sub>4</sub>//AC capacitor device exhibited a maximum energy density of approximately 59.5 W h kg<sup>-1</sup> at a power density of 1000 W kg<sup>-1</sup> and maintained a substantial energy density of 28.4 W h kg<sup>-1</sup> at the power density of 4000 W kg<sup>-1</sup>. This value is higher than those of previously reported ASCs such as NiCo<sub>2</sub>S<sub>4</sub>-rGO (16%)//NCCF-rGO,<sup>15</sup> Ni<sub>1</sub>-Co<sub>2</sub>-S/Co(OH)<sub>2</sub>//AC,<sup>18</sup> Co<sub>3</sub>S<sub>4</sub>/CoMo<sub>2</sub>S<sub>4</sub>-rGO//AC,<sup>19</sup> AC//Ni-Co-S,<sup>36</sup> MoO<sub>3</sub>/NiMoO<sub>4</sub>//AC,<sup>37</sup> AC/Co(OH)<sub>2</sub>/Ni

foam,<sup>38</sup> NF/S-Co<sub>3</sub>O<sub>4</sub>@NiCo<sub>2</sub>S<sub>4</sub>//AC,<sup>39</sup> NiS/MoS<sub>2</sub>//AC,<sup>40</sup> and Mo-CuO-2//AC.<sup>41</sup> These exciting results indicate that the hierarchical Co(OH)<sub>2</sub>@NiMoS<sub>4</sub> nanocomposite is a promising material for high-performance electrodes.

## Conclusion

Hierarchical Co(OH)<sub>2</sub>/NiMoS<sub>4</sub> nanocomposites were synthesised on a carbon cloth by a two-step hydrothermal method coupled with a vulcanization method. The resulting nanocomposites are composed of large-scale interlaced Co(OH)<sub>2</sub> nanowires covered with dense NiMoS<sub>4</sub> nanoflakes. As a novel electrode material for pseudo-capacitors, the nanocomposite exhibited excellent electrochemical properties, with a high specific capacitance of 2229 F g<sup>-1</sup> at a current density of 1 A g<sup>-1</sup>. An ASC fabricated using the as-synthesised nanocomposite as the positive electrode and AC as the negative electrode exhibited a maximum energy density of 59.5 W h kg<sup>-1</sup> at a power density of 1 kW h kg<sup>-1</sup> and excellent cycling stability. These results indicate that the hierarchical Co(OH)<sub>2</sub>@NiMoS<sub>4</sub> nanocomposite has the potential for application in energy storage devices.

## Conflicts of interest

There are no conflicts to declare.

## Acknowledgements

This work was supported by the Natural Science Foundation Project of CQ CSTC (Grant No. cstc2019jcyj-msxmX0311) and the Fundamental Research Funds for the Central Universities (grant XDJK2018B033 and XDJK2020B055).

## References

- 1 J. R. Miller and P. Simon, Materials science–electrochemical capacitors for energy management, *Science*, 2008, **321**, 651–652.
- 2 P. Simon and Y. Gogotsi, Materials for electrochemical capacitors, *Nat. Mater.*, 2008, **7**, 845–854.
- 3 G. P. Xiong, P. G. He, Z. P. Lyu, T. F. Chen, B. Y. Huang, L. Chen and T. S. Fisher, Bioinspired leaves-on-branchlet hybrid carbon nanostructure for supercapacitors, *Nat. Commun.*, 2018, **9**, 790.
- 4 W. Wen, J. C. Yao, H. Tan and J. M. Wu, Hollow TiN nanotrees derived from a surface induced Kirkendall effect and their application in high-power supercapacitors, *J. Mater. Chem. A*, 2019, **7**, 21378.
- 5 Y. J. Gu, W. Wen and J. M. Wu, Simple air calcination affords commercial carbon cloth with high areal specific capacitance for symmetrical supercapacitors, *J. Mater. Chem. A*, 2018, **6**, 21078.
- 6 Z. Yu, L. Tetard, L. Zhai and J. Thomas, Supercapacitor electrode materials: nanostructures from 0 to 3 dimensions, *Energy Environ. Sci.*, 2015, **8**, 702–730.





- 7 C. B. Duan, J. W. Zhao, L. R. Qin, L. J. Yang and Y. C. Zhou, Ternary Ni-Co-Mo oxy-hydroxide nanoflakes grown on carbon cloth for excellent supercapacitor electrodes, *Mater. Lett.*, 2017, **208**, 65–68.
- 8 G. Liu, B. Wang, L. Wang, T. Liu, T. Gao and D. Wang, Facile controlled synthesis of a hierarchical porous nanocoral-like  $\text{Co}_3\text{S}_4$  electrode for high-performance supercapacitors, *RSC Adv.*, 2016, **6**, 54076–54086.
- 9 D. Kong, C. Cheng, Y. Wang, J. I. Wong, Y. Yang and H. Y. Yang, Three-dimensional  $\text{Co}_3\text{O}_4@\text{C}@\text{Ni}_3\text{S}_2$  sandwich-structured nanoneedle arrays: towards high-performance flexible all-solid-state asymmetric supercapacitors, *J. Mater. Chem. A*, 2015, **3**, 16150–16161.
- 10 Y. Yang, H. Fei, G. Ruan, C. Xiang and J. M. Tour, Edge-oriented  $\text{MoS}_2$  nanoporous films as flexible electrodes for hydrogen evolution reactions and supercapacitor devices, *Adv. Mater.*, 2014, **26**, 8163–8168.
- 11 X. Y. Yu and X. W. Lou, Mixed metal sulfides for electrochemical energy storage and conversion, *Adv. Energy Mater.*, 2018, **8**, 1701592.
- 12 X. M. Geng, Y. L. Zhang, Y. Han, J. Li, L. Yang, M. Benamara, L. Chen and H. L. Zhu, Two-dimensional water-coupled metallic  $\text{MoS}_2$  with nanochannels for ultrafast supercapacitors, *Nano Lett.*, 2017, **17**, 1825–1832.
- 13 L. Li, H. Hu, S. Ding, X. Yan and C. Wang,  $\text{CoNi}_2\text{S}_4$  nanosheets on nitrogen-doped carbon foam as binder-free and flexible electrodes for high-performance asymmetric supercapacitors, *Nanotechnology*, 2019, **30**, 495404.
- 14 H. C. Chen, J. J. Jiang, L. Zhang, H. Z. Wan, T. Qi and D. D. Xia, Highly conductive  $\text{NiCo}_2\text{S}_4$  urchin-like nanostructures for high-rate pseudocapacitors, *Nanoscale*, 2013, **5**, 8879–8883.
- 15 Y. M. Fan, Y. C. Liu, X. B. Liu, Y. N. Liu and L. Z. Fan, Hierarchical porous  $\text{NiCo}_2\text{S}_4$ -rGO composites for high-performance supercapacitors, *Electrochim. Acta*, 2017, **249**, 1–8.
- 16 D. Du, R. Lan, J. Humphreys, W. Xu, K. Xie, H. Wang and S. Tao, Synthesis of  $\text{NiMoS}_4$  for high-performance hybrid supercapacitors, *J. Electrochem. Soc.*, 2017, **164**, A2881–A2888.
- 17 X. F. Wang, Y. F. Zhang, J. Q. Zheng, X. Liu and C. G. Meng, Hydrothermal synthesis of  $\text{VS}_4/\text{CNTs}$  composite with petal-shape structures performing a high specific capacity in a large potential range for high-performance symmetric supercapacitors, *J. Colloid Interface Sci.*, 2019, **554**, 191–201.
- 18 T. H. Xu, G. Y. Li and L. J. Zhao, Ni-Co-S/Co(OH) $_2$  nanocomposite for high energy density all-solid-state asymmetric supercapacitors, *Chem. Eng. J.*, 2018, **336**, 602–611.
- 19 X. Yang, H. Sun, P. Zan, L. Zhao and J. Lian, Growth of vertically aligned  $\text{Co}_3\text{S}_4/\text{CoMo}_2\text{S}_4$  ultrathin nanosheets on reduced graphene oxide as a high-performance supercapacitor electrode, *J. Mater. Chem. A*, 2016, **4**, 18857–18867.
- 20 F. S. Chen, H. Wang, S. Ji, B. G. Pollet and R. F. Wang, Hierarchical core-shell structured  $\text{CoNi}_2\text{S}_4/\text{Ni}_3\text{S}_2@\text{Ni}(\text{OH})_2$  nanosheet arrays as electrode for electrochemical energy storage, *J. Alloys Compd.*, 2019, **785**, 684–691.
- 21 T. Zhao, H. Jiang and J. Ma, Surfactant-assisted electrochemical deposition of  $\alpha$ -cobalt hydroxide for supercapacitors, *J. Power Sources*, 2011, **196**, 860–864.
- 22 Z. Yu, Z. Cheng, S. R. Majid, Z. Tai, X. Wang and S. Dou, Smart design of free-standing ultrathin Co-Co(OH) $_2$  composite nanoflakes on 3D nickel foam for high-performance electrochemical capacitors, *Chem. Commun.*, 2015, **51**, 1689–1692.
- 23 S. M. Li, H. Jiang, K. Yang, Z. Zhang, S. J. Li, N. H. Luo, Q. H. Liu and R. Wei, Three-dimensional hierarchical graphene/ $\text{TiO}_2$  composite as highperformance electrode for supercapacitor, *J. Alloys Compd.*, 2018, **746**, 670–676.
- 24 S. M. Li, K. Yang, P. W. Ye, H. Jiang, Z. Zhang, Q. Huang and L. Y. Wang, Hierarchical interpenetrating rHGO-decorated  $\text{NiCo}_2\text{O}_4$  nanowires architectures for high-performance supercapacitors, *Appl. Surf. Sci.*, 2019, **473**, 326–333.
- 25 Z. J. Fan, J. Yan, T. Wei, L. J. Zhi, G. Q. Ning, T. Y. Li and F. Wei, Asymmetric supercapacitors based on graphene/ $\text{MnO}_2$  and activated carbon nanofiber electrodes with high power and energy density, *Adv. Funct. Mater.*, 2011, **21**, 2366–2375.
- 26 X. Wu, L. Jiang, C. Long, T. Wei and Z. Fan, Dual support system ensuring porous Co-Al hydroxide nanosheets with ultrahigh rate performance and high energy density for supercapacitors, *Adv. Funct. Mater.*, 2015, **25**, 1648–1655.
- 27 M. Gao, K. Le, D. Xu, Z. Wang, F. Wang, W. Liu, H. Yu, J. Liu and C. Chen, Controlled sulfidation towards achieving core-shell 1D- $\text{NiMoO}_4@2\text{DNiMoS}_4$  architecture for high-performance asymmetric supercapacitor, *J. Alloys Compd.*, 2019, **804**, 27–34.
- 28 Y. Zhao, X. He, R. Chen, Q. Liu, J. Liu, J. Yu, J. Li, H. Zhang, H. Dong, M. Zhang and J. Wang, A flexible all-solid-state asymmetric supercapacitors based on hierarchical carbon cloth@ $\text{CoMoO}_4@/\text{NiCo}$  layered double hydroxide core-shell heterostructures, *Chem. Eng. J.*, 2018, **352**, 29–38.
- 29 S. Kumar, G. Saeed, N. H. Kim and J. H. Lee, Hierarchical nanohoneycomb-like  $\text{CoMoO}_4\text{-MnO}_2$  core-shell and  $\text{Fe}_2\text{O}_3$  nanosheet arrays on 3D graphene foam with excellent supercapacitive performance, *J. Mater. Chem. A*, 2018, **6**, 7182–7193.
- 30 F. Lai, Y. Huang, Y. E. Miao and T. Liu, Controllable preparation of multi-dimensional hybrid materials of nickel-cobalt layered double hydroxide nanorods/nanosheets on electrospun carbon nanofibers for high-performance supercapacitors, *Electrochim. Acta*, 2015, **174**, 456–463.
- 31 Y. Cao, L. An, L. Liao, X. Liu, T. Ji, R. Zou, J. Yang, Z. Qin and J. Hu, Hierarchical core/shell structures of  $\text{ZnO}$  nanorod@ $\text{CoMoO}_4$  nanoplates used as a high-performance electrode for supercapacitors, *RSC Adv.*, 2016, **6**, 3020–3024.
- 32 W. Wang, L. Yang, F. Qu, Z. Liu, G. Du, A. M. Asiri, Y. Yao, L. Chen and X. Sun, A self-supported  $\text{NiMoS}_4$  nanoarray as an efficient 3D cathode for the alkaline hydrogen evolution reaction, *J. Mater. Chem. A*, 2017, **5**, 16585–16589.



- 33 J. X. Wang, J. W. Zhao, L. R. Qin, B. L. Zhao and Z. Y. Jiang, Synthesis of ordered Ni/NiO nanocables for electrochemical capacitor application, *J. Nanopart. Res.*, 2018, **20**, 90.
- 34 X. J. Ma, L. B. Kong, W. B. Zhang, M. C. Liu, Y. C. Luo and L. Kang, Design and synthesis of 3D  $\text{Co}_3\text{O}_4@\text{MMoO}_4$  ( $\text{M}=\text{Ni}, \text{Co}$ ) nanocomposites as high-performance supercapacitor electrodes, *Electrochim. Acta*, 2014, **130**, 660–669.
- 35 X. He, R. Li, J. Liu, Q. Liu, R. Chen, D. Song and J. Wang, Hierarchical  $\text{FeCo}_2\text{O}_4@\text{NiCo}$  layered double hydroxide core/shell nanowires for high performance flexible all-solid-state asymmetric supercapacitors, *Chem. Eng. J.*, 2018, **334**, 1573–1583.
- 36 Z. Wang, H. Wang, S. Ji, H. Wang, D. J. L. Brett and R. Wang, Design and synthesis of tremella-like Ni-Co-S flakes on co-coated cotton textile as high-performance electrode for flexible supercapacitor, *J. Alloys Compd.*, 2020, **814**, 151789.
- 37 X. Y. Zhang, L. Wei and X. Guo, Ultrathin mesoporous  $\text{NiMoO}_4$ -modified  $\text{MoO}_3$  core/shell nanostructures: enhanced capacitive storage and cycling performance for supercapacitors, *Chem. Eng. J.*, 2018, **353**, 615–625.
- 38 M. Li, S. Xu, C. Cherry, Y. Zhu, R. Huang, R. Qi, P. Yang, L. Wang and P. K. Chu, Asymmetrical Supercapacitor Composed of Thin  $\text{Co}(\text{OH})_2$  Nanoflakes on Three-Dimensional Ni/Si Microchannel Plates with Superior Electrochemical Performance, *Electrochim. Acta*, 2014, **149**, 18–27.
- 39 Y. Ouyang, H. T. Ye, X. F. Xia, X. Y. Jiao, G. M. Li, S. Mutahir, L. Wang, D. Mandler, W. Lei and Q. L. Hao, Hierarchical electrodes of  $\text{NiCo}_2\text{S}_4$  nanosheets anchored sulfur-doped  $\text{Co}_3\text{O}_4$  nanoneedles with advanced performance for battery-supercapacitor hybrid devices, *J. Mater. Chem. A*, 2019, **7**, 3228–3237.
- 40 J. Yan, S. C. Wang and Y. Chen, Smart in situ construction of  $\text{NiS}/\text{MoS}_2$  composite nanosheets with ultrahigh specific capacity for high-performance asymmetric supercapacitor, *J. Alloys Compd.*, 2019, **811**, 151915.
- 41 W. B. Lv, L. Li, Q. H. Meng and X. T. Zhang, Molybdenum-doped  $\text{CuO}$  nanosheets on Ni foams with extraordinary specific capacitance for advanced hybrid supercapacitors, *J. Mater. Sci.*, 2020, **55**, 2492–2502.

